

In situ pore-scale analysis of oil recovery during three-phase near-miscible CO₂ injection in a water-wet carbonate rock

Abdulla Alhosani ^{a,*}, Alessio Scanziani ^a, Qingyang Lin ^a, Ziqing Pan ^b, Branko Bijeljic ^a, Martin J. Blunt ^a

^a Imperial College London, Department of Earth Science and Engineering, London, UK

^b Imperial College London, Department of Chemical Engineering, London, UK



ARTICLE INFO

Keywords:

Three-phase flow
Enhanced oil recovery (EOR)
Near miscible
X-ray imaging
CO₂ gas injection
Oil layers
Micro-CT
Pore occupancy

ABSTRACT

We study *in situ* three-phase near-miscible CO₂ injection in a water-wet carbonate rock at elevated temperature and pressure using X-ray microtomography. We examine the recovery mechanisms, presence or absence of oil layers, pore occupancy and interfacial areas during a secondary gas injection process. In contrast to an equivalent immiscible system, we did not observe layers of oil sandwiched between gas in the centre of the pore space and water in the corners. At near-miscible conditions, the measured contact angle between oil and gas was approximately 73°, indicating only weak oil wettability in the presence of gas. Oil flows in the centres of large pores, rather than in layers for immiscible injection, when displaced by gas. This allows for a rapid production of oil since it is no longer confined to movement in thin layers. A significant recovery factor of 80% was obtained and the residual oil saturation existed as disconnected blobs in the corners of the pore space. At equilibrium, gas occupied the biggest pores, while oil and water occupied pores of varying sizes (small, medium and large). Again, this was different from an immiscible system, where water occupied only the smallest pores. We suggest that a double displacement mechanism, where gas displaces water that displaces oil is responsible for shuffling water into larger pores than that seen after initial oil injection. This is only possible since, in the absence of oil layers, gas can contact water directly. The gas-oil and oil-water interfacial areas are lower than in the immiscible case, since there are no oil layers and even water layers in the macro-pore space become disconnected; in contrast, there is a larger direct contact of oil to the solid. These results could serve as benchmarks for developing near-miscible pore-scale modelling tools.

1. Introduction

Miscible flooding is an attractive option for many producing oil reservoirs that are experiencing a rapid decline in pressure and/or production from water injection. However, the achievement of miscibility may require high injection pressures, or enriched gases, both of which are expensive or operationally difficult; in contrast, near-miscible flooding may be cheaper and easier to implement (Shyeh-Yung, 1991). Near-miscible injection refers to the injection of gases at pressures slightly lower than the minimum miscibility pressure (MMP). Such conditions result in a low but not negligible interfacial tension between the gas and oil phases (~ 1 mN/m). Many laboratory studies and some field implementations suggest that near-miscible and miscible injection perform in a comparable manner (Chen et al., 2017).

Shyeh-Yung (1991) conducted 33 near-miscible CO₂ core flooding experiments in both Berea sandstone and a Texas carbonate at reservoir conditions. The author reported that the change in tertiary oil recovery

is minimal when switching from miscible to near-miscible conditions. They attributed the substantial oil recovery at near-miscible conditions to the low gas-oil interfacial tension which enhances the sweep efficiency and reduces pore level bypassing. These results contradict the severe decline in oil recovery the author observed from slim tube tests as the pressure dropped below the minimum miscibility pressure. These findings suggest that slim tube tests do not provide realistic data at near-miscible pressures, and whenever possible must be replaced with reservoir condition core floods.

Similarly, Schechter et al. (1998) carried out extensive CO₂ core flooding experiments to optimize the performance of the EOR gas injection scheme in the Wellman unit. In their study, they considered dropping the reservoir pressure to reduce the injected volume of CO₂. In addition, they performed field scale simulations to characterize the sweep efficiency at lower pressures. They found out that maintaining the pressure slightly below the MMP did not reduce oil recovery; meanwhile the field scale simulations suggested optimum sweep efficiency at

* Corresponding author.

E-mail address: abdulla.alhosani17@imperial.ac.uk (A. Alhosani).

these conditions. Further experimental evidence provided by [Grigg and Schechter \(1997\)](#) showed that oil recovery can still be quite high at pressures slightly below the MMP.

Near-miscible core flood tests were complemented by field-scale simulations to help justify the substantial oil recovery observed at these conditions ([Burger et al., 1994](#); [Pande, 1992](#); [Thomas et al., 1994](#)). [Burger et al. \(1994\)](#) and [Thomas et al. \(1994\)](#) simulated 2D miscible and near-miscible injection processes in heterogeneous reservoirs. Both authors reported a higher oil recovery for the near-miscible schemes which was attributed to their improved sweep efficiencies. [Pande \(1992\)](#) demonstrated from a compositional simulation that the gravity and viscous cross flow processes occurring at near-miscible conditions are the reasons behind the increased sweep efficiency. Overall, these studies indicate that a better sweep efficiency may be possible from near-miscible flooding, combined with operational cost savings. However, they do not address the impact of near-miscible conditions on local displacement efficiency.

In light of these promising results reported in near-miscible studies, many authors have investigated the microscopic mechanisms of oil recovery under these conditions ([Sohrabi et al., 2008](#); [Jamiolahmady et al., 2000](#); [Williams and Dawe, 1988](#); [Bui et al., 2010](#); [Wylie and Mohanty, 1997](#)). While most authors focussed on understanding the phase behaviour of the fluids and quantifying the mass transfer mechanisms, only few tried to visualize the pore-scale dynamics. Understanding the pore-scale dynamics is essential to predict how the three-phases (oil, water and gas) flow simultaneously at equilibrium conditions (e.g. further away from the well).

[Williams and Dawe \(1988\)](#) photographed near critical liquid-liquid mixtures in a transparent porous medium. They concluded that at very low interfacial tensions between gas and oil, the two phases can flow alongside each other in the same pore. [Sohrabi et al. \(2008\)](#) imaged high pressure equilibrated gas-oil-water flow experiment in a 2D water-wet micromodel. They also observed the flow of oil and gas along the same path in a single pore. Their micromodel images indicate that as the gas front propagates through the porous medium, the oil recovery continues by cross-flow from the bypassed pores into the main flow stream which results in a high oil recovery.

The observations of [Williams and Dawe \(1988\)](#) and [Sohrabi et al. \(2008\)](#) indicate that in a water-wet medium, oil flows in the centre of the larger pores alongside the gas phase at near-miscible conditions. This contradicts the typical wettability order observed for water-wet media, where water occupies the smallest pores, gas the biggest, while oil spreads in layers occupying pores of intermediate size ([Blunt, 2017](#)). Hence, it appears that lowering the oil-gas interfacial tension at near-miscible conditions leads to a break-down in the strict wettability order in the system, as oil is no longer confined to movement in layers (oil does not spread in layers between gas and water) and is allowed to flow rapidly in the centre of the larger pores.

The impact that lowering the interfacial tension (i.e. near-miscible conditions) has on relative permeability was highlighted in a study conducted by [Longeron \(1980\)](#). [Longeron \(1980\)](#) measured two phase relative permeability in a vapour-liquid system and observed that lowering the interfacial tension between the fluids increased the relative permeability of the two phases. As the mixture approached miscibility (near-miscible conditions), the relative permeabilities approached a straight line. Intuitively, the displacement of oil by gas in the larger pores at near-miscible conditions will result in a higher oil relative permeability compared to the case where oil is displaced in medium-sized pores. Furthermore, lowering the interfacial tension decreases the capillary pressure between the displacing and the displaced fluids. This suggests that gas can easily displace oil in the pore space at near-miscible conditions (i.e. improved microscopic displacement efficiency). The combination of oil phase flowing in the larger pores and the improved gas displacement efficiency could justify the more favourable oil recovery observed at near-miscible conditions.

Nevertheless, before drawing any definitive conclusions, we must note that this phenomenon of oil flowing in the larger pores in the presence of gas was only observed in micromodels and there is no evidence of it occurring in real rock systems. [Scanziani et al. \(2018b\)](#) were the first to directly visualize the *in situ* wettability order at high temperature and pressure in a water-wet rock during immiscible gas flooding using three-dimensional micro-CT images. They demonstrated how advanced micro-CT imaging techniques can quantify and visualize the different pore-scale processes taking place during multiphase flow experiments.

While *in situ* micro-CT studies of immiscible gas injection have been reported ([Moghadasi et al., 2016](#); [Scanziani et al., 2018a](#); [Scanziani et al., 2018b](#)), there is a deficiency in the literature for near-miscible studies. This is attributed to the complexity of visualising the gas and oil phases at low interfacial tensions. At lower interfacial tensions, the gas and oil tend to have similar properties which makes it difficult to distinguish the two phases in the micro-CT image. Therefore, the design of the experiment must be tailored to permit the visualisation of the of the pore-scale level mechanisms.

In this work, we conduct a three-phase near-miscible micro-CT flow experiment in a water-wet carbonate rock at elevated temperature and pressure (70 °C and 10.85 MPa). We examine (i) oil recovery mechanisms, (ii) whether or not oil layers are present, (iii) pore occupancy, (iv) fluid-fluid interfacial areas, and (v) double displacement processes at near-miscible conditions. We compare the results to those at immiscible conditions. This will help directly visualize the predicted wettability order at near-miscible conditions, as well as confirm the presence or absence of oil layers.

2. Materials and methods

2.1. Materials

The rock sample selected for the study was a Ketton limestone (composition: >99% calcite), with a diameter of 5.9 mm and a length of 24.4 mm. The structure of Ketton is comprised of spherical grains with large pore spaces and micro-pores within the grains themselves. The size of micro-pores is typically lower than that of a micro-CT image resolution and therefore is impossible to capture using traditional segmentation methods ([Bijeljic et al., 2013](#); [Blunt, 2017](#)). Hence, we used the differential imaging method, comparing a dry scan with one where the rock is completely saturated with a high-contrast brine, proposed by [Lin et al. \(2016\)](#) and applied in [Bijeljic et al. \(2018\)](#) to characterize the total porosity of the Ketton sample. The total porosity was measured to be 29%, with macro-porosity and micro-porosity accounting for 15% and 14% respectively, see [Fig. 1](#). Finally, the sample was cleaned using methanol and dried in a vacuum oven at 90 °C for 72 h prior to conducting the experiment.

The three fluid phases selected to perform the near-miscible gas injection experiment were: (i) supercritical (sc) CO₂ as the gas phase, (ii) decane as the oil phase and (iii) reservoir brine as the water phase. However, to enhance the contrast between the fluids in the micro-CT images, the water and oil phases were doped. The choice of fluid dopants was driven by a trade-off between enhancing the X-ray attenuation contrast and preserving the original fluid composition. The water phase was doped with a 30% wt solution of sodium iodide: sodium iodide is preferred since iodine absorbs X-rays strongly, and natural brines are predominantly sodium chloride ([Vinegar and Wellington, 1987](#)), while decane was doped with a 20% wt iododecane solution. The optimum doping concentrations were judged with phase contrast scans and signal-to-noise ratio intensity histograms (Figure S1 in the supplementary material).

The interfacial tension between the gas phase (scCO₂) and the oil phase (80% wt decane and 20% wt iododecane mixture) was measured using the pendant drop method, with the two phases in thermodynamic equilibrium. The apparatus for performing the pendant drop interfacial tension measurements at high temperatures and

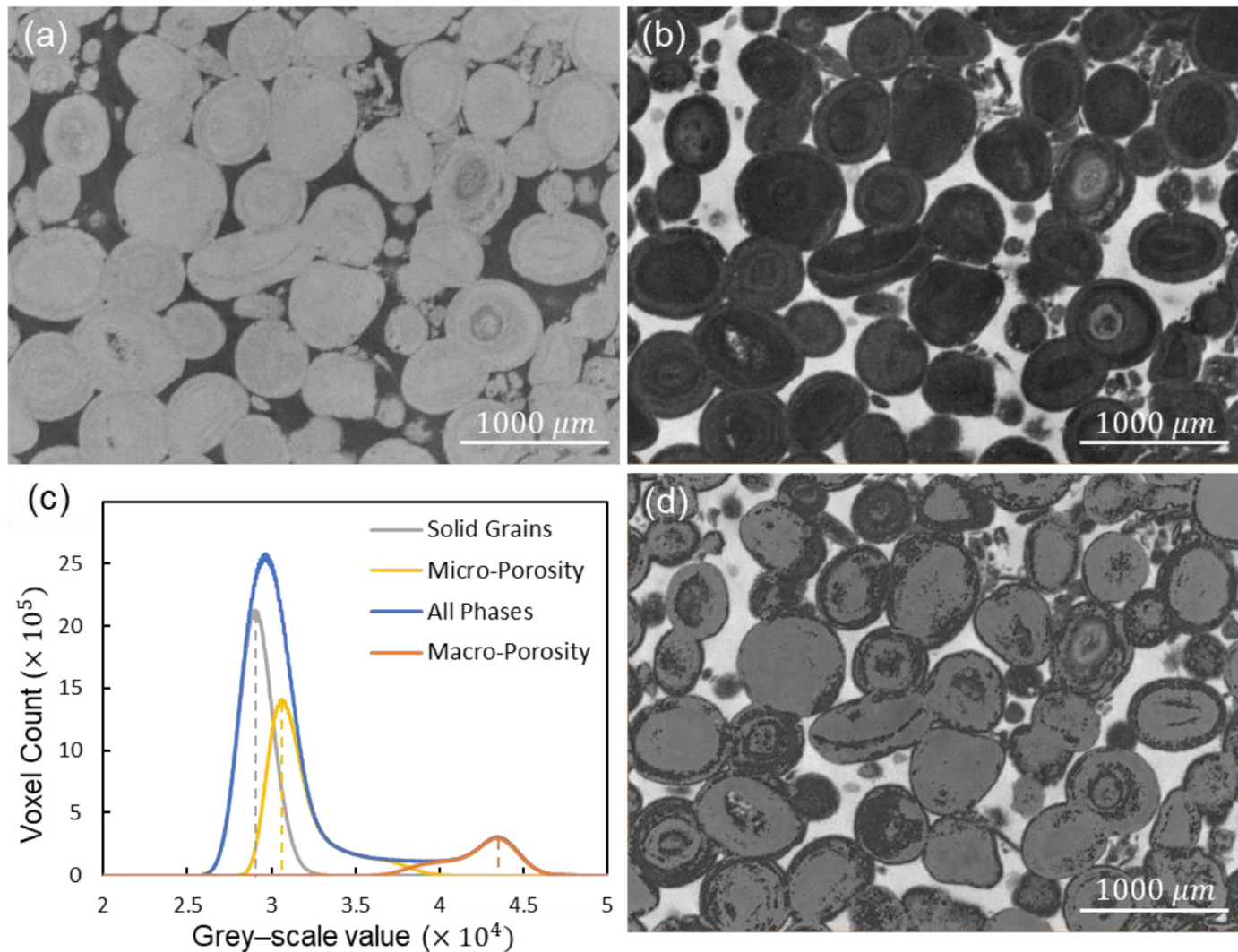


Fig. 1. (a) A two-dimensional slice of a 3D image for the dry scan of the Ketton sample with a $3.57 \mu\text{m}$ voxel size. (b) A 2D slice of the differential image of the Ketton sample obtained by subtracting the grey-scale values of the high-contrast brine saturated scan from the dry scan in (a). (c) The histogram plot of the three-phases (macro-porosity, micro-porosity and solid grains) in the water injection scan. The dashed lines represent the peak grey-scale value for each phase (CT). Micro-porosity is calculated using $\phi_{\text{micro}} = (CT_{\text{micro}} - CT_{\text{grain}})/(CT_{\text{macro}} - CT_{\text{grain}})$ to be 14%, while macro-porosity was found to be 15% giving a total sample porosity of 29%. (d) A segmented image of the Ketton sample showing: in grey the solid grains, white the macro-porosity and black the micro-porosity.

high pressures is described elsewhere (Li et al., 2012). The pendant drop profile was digitized using the automated axisymmetric drop shape analysis (ADSA), which calculates the interfacial tension using the Young-Laplace equation. We measured the interfacial tensions between oil and gas phases at a temperature of 70°C and pressures up to 6 MPa . The measured interfacial tension values are shown in Fig. 2. According to Georgiadis et al. (2010), at a temperature of 70°C , the relationship between the interfacial tension of scCO₂ and decane system against pressure (ranging from 0 to 9 MPa) is given by a simple linear function: we were not able to measure directly the low interfacial tension at the experimental pressure, but had to use extrapolation. Hence, by fitting a linear regression line through the data, the interfacial tension measurements were extrapolated down to the minimum miscibility pressure (MMP). Therefore, to achieve near-miscible gas-oil conditions ($\sim 1\text{ mN/m}$), the experiment was conducted at a temperature of 70°C and a pressure of 10.85 MPa . The interfacial tensions, viscosities and densities of the three fluid phases are listed in Table 1.

2.2. Methods

2.2.1. Flow Loop

The experimental apparatus used to conduct the flow experiment is shown in Fig. 3. The apparatus consisted of four Teledyne Isco pumps connected to a Parr stirred reactor and a Hassler type carbon fibre core-holder. The stirred reactor was used to equilibrate the scCO₂, brine and rock phases at the experimental conditions (70°C and 10.85 MPa) to avoid mass transfer during the experiment and replicate reservoir conditions further away from the injection site. The fluids were vigorously mixed in the reactor for at least 12 h prior to injection to ensure that chemical equilibrium was attained.

The coreholder was placed inside the micro-CT scanner for image acquisition. The rock sample was centred in the middle of the coreholder. The sample was connected to the flow lines by two steel end pieces placed at the inlet and outlet of the rock. Prior to inserting the sample in the coreholder, it was wrapped with a PTFE tape, then aluminium foil and placed in a Viton sleeve. All flow lines were made of

Table 1

Thermophysical properties of the three fluid phases selected for the experiment. Data from Georgiadis et al. (2010), Heidaryan et al. (2011), and NIST (2019).

Fluid	Composition [%wt]	ρ [kg · m ⁻³]	μ [mP · as]	σ [mN · m ⁻¹]
Water	(70% brine + 30% Sodium Iodide)	1414.9*	–	$\sigma_{gw} = 31$
Oil	(80% decane + 20% iododecane)	796.8*	1.12	$\sigma_{ow} = 30$
Gas	scCO ₂	530.8	0.04	$\sigma_{go} = 1$

* Densities measured at ambient conditions.

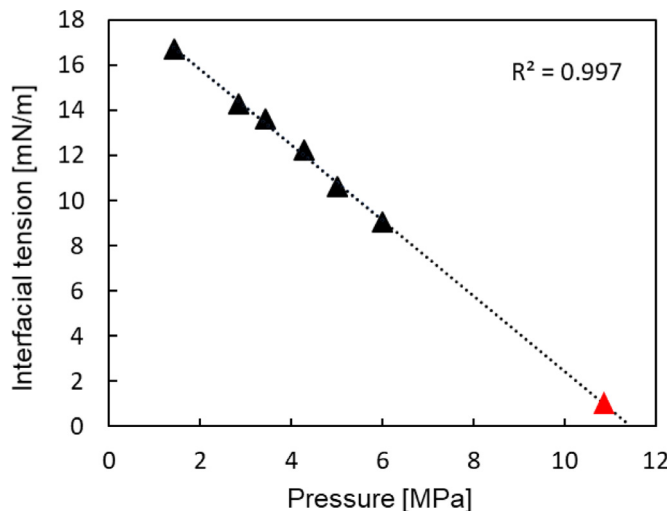


Fig. 2. Interfacial tension measurements between the gas phase (scCO₂) and the oil phase (80% wt decane and 20% wt iododecane mixture) as a function of pressure at 70 °C. The black triangles represent the experimentally measured interfacial tension values (Table S1 in the supplementary material), while the red triangle represents our selected near-miscible experimental conditions (10.85 MPa) based on the extrapolated data.

thermoplastic 1/16th PEEK tubing which can withstand high pressures and temperatures.

The sample was first flushed with non-equilibrated brine at 0.1 mL/min to displace the air and dissolve any pre-existing CO₂ in the system. The pressure of the non-equilibrated brine in the system was raised gradually to the reactor pressure (10.85 MPa), and the confining pressure to 12.3 MPa. A confining pressure was applied to prevent fluid bypassing along the sample walls. The sample temperature was then raised to the reactor temperature (70 °C) using an Omega flexible heater connected to a PID controller. The electrical heater was wrapped around the carbon fibre coreholder with a separate thermocouple placed near the sample to monitor the temperature during the experiment.

2.2.2. Flooding Sequence

The flooding sequence in the experiment follows an EOR secondary gas injection strategy: (i) water injection to start with a fully-saturated pore space, (ii) oil injection, representing primary oil migration, and (iii) gas injection. The secondary gas injection strategy was selected to maximise the number of interfaces between gas and oil phases to closely examine the near-miscible gas injection phenomenon. The experiments were performed under capillary dominated conditions to mimic the displacement mechanism in the subsurface. Firstly, 50 pore volumes (PV) of equilibrated brine were injected at a flowrate of 0.1 mL/min to displace the non-equilibrated brine and ensure 100% equilibrated brine saturation at the start of the experiment. Then, 5 PV of oil were injected into the sample at a flowrate of 0.008 mL/min for 100 mins to simulate a drainage process. Finally, equilibrated scCO₂ was injected into the sample at a rate of 0.008 mL/min, simulating a secondary recovery process, with a total volume corresponding to 3 PV. All injections

Table 2

Details of the experimental injection sequence. PV stands for the pore volume of the sample. The capillary number was calculated using $Ca = \mu q / \sigma$, where σ is the interfacial tension between oil and water for oil injection and gas and oil for gas injection, μ is the viscosity of the displacing fluid and q is the Darcy velocity. σ and μ are shown in Table 1, while q is calculated by dividing the flow rate by the cross-sectional area of the sample.

Injection sequence	PV injected	Flow rate [mL/min]	Capillary number
Water	50	0.1	–
Oil	5	0.008	1.76×10^{-7}
Gas	3	0.008	1.89×10^{-7}

Table 3

The imaging parameters used in the micro-CT. A large number of projections and a long exposure time were needed for the saturated scans to increase the image quality.

Scan	Projections	Exposure time [s]	Scanning time [min]
Dry	2400	1	76×4
Water injection	3201	1.75	142×4
Oil injection	3201	1.75	142×4
Gas injection	3201	1.75	142×4

were performed at the bottom of the sample. Injection details including capillary number values are provided in Table 2.

2.2.3. Image Acquisition

The ZEISS Xradia 510 Versa micro-CT scanner was used to acquire three-dimensional images of the rock sample and the injected fluids. The photon energy range in the micro-CT was set to (20–80) keV with a power of 7 W. A 3000 × 2000 (pixels) flat panel extension was employed at the detector to maximize the field of view while increasing the image resolution. Four scans with a resolution of 3.57 μm per voxel were acquired at different heights to image the whole sample after each injection step. The saturated scans required more projections and exposure time compared to the dry scan. Details regarding number of projections, exposure and scanning times are provided in Table 3.

2.2.4. Image Processing

The images were reconstructed and a cylindrical mask equivalent in diameter to the rock sample was applied to discard any unwanted regions including the Viton sleeve and the aluminium foil, see Fig. 4. The four scans of each injection step were then stitched to build three-dimensional images of the whole rock sample (Fig. 4e). The stitched images containing fluids were then registered to the dry scan, to allow for a direct pore-by-pore comparison after each injection step.

A non-local means filter was applied to the pore-scale images to reduce the noise, allowing for a more accurate subsequent segmentation process. The segmentation was performed using the seeded watershed algorithm (Jones et al., 2005). This allowed us to overcome misclassification at the fluid boundaries caused by the partial volume effect (Brown et al., 2014). The seeded watershed algorithm relies on a gradient magnitude versus image intensity histogram. First, each phase is assigned a grey-scale value range. Then, the intensity gradient for each phase is identified, at the boundaries, to demarcate the exact location

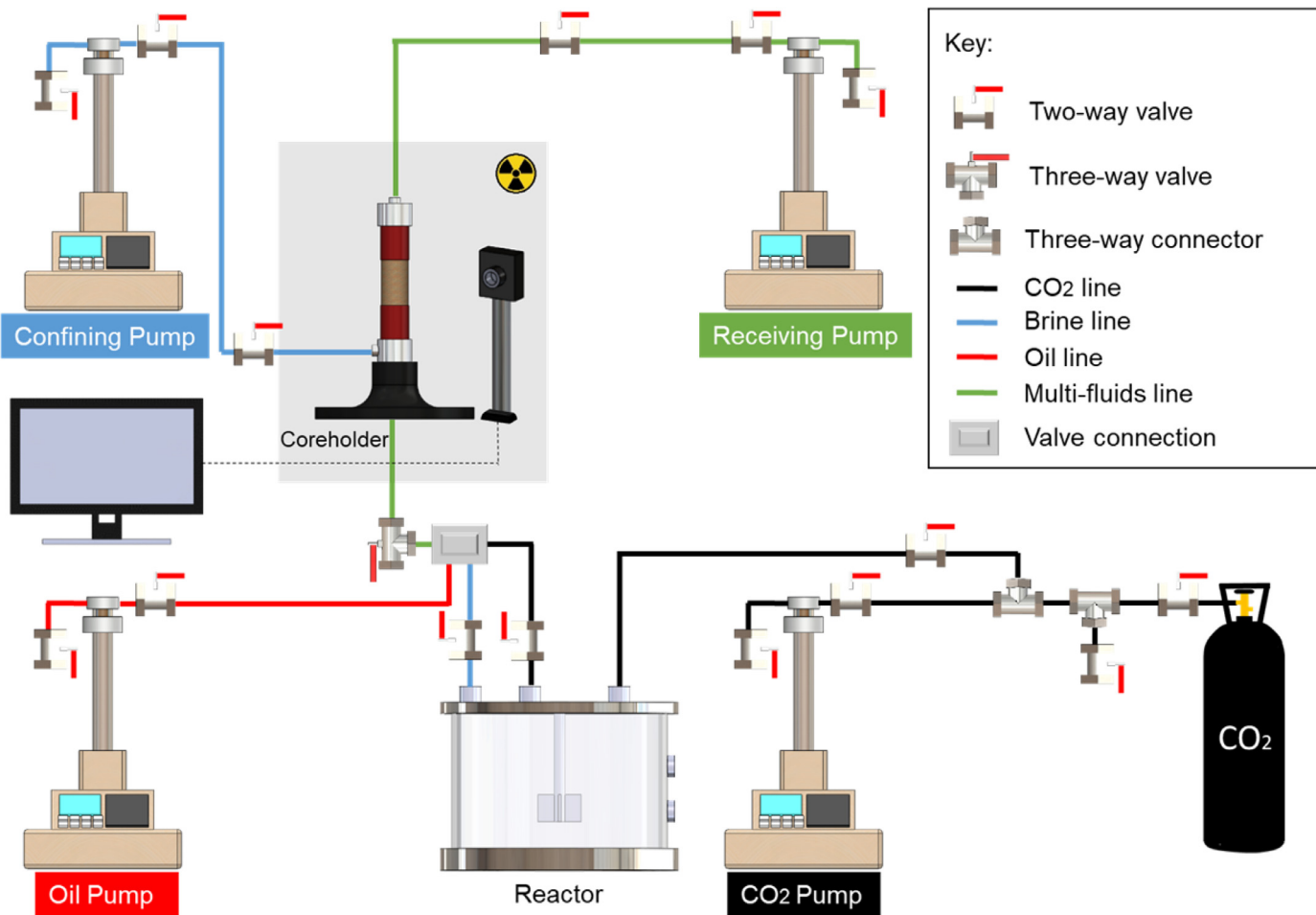


Fig. 3. The high-pressure, high-temperature flow apparatus used to perform the experiment. The apparatus consisted of four syringe pumps, stirred reactor, CO₂ cylinder, coreholder and a micro-CT scanner. The shaded area represents the micro-CT X-ray enclosure.

of the fluid interfaces. The homogenous region of each phase (high certainty regions) is flooded with seeds, these seeds are then grown proportionally to a certain gradient value, and the two phases meet at the steepest intensity point 'hill slope' (Sheppard et al., 2004). Additional details on image processing are provided in the Supplementary Material.

2.2.5. Oil Layers

2.2.5.1. Capillary Pressure analysis. From Table 1, we can see that the spreading coefficient ($C_s = \sigma_{gw} - \sigma_{ow} - \sigma_{go}$) is approximately zero. This suggests that oil layers can form, sandwiched between gas in the centres of the pores and water in the corners of the pore space (Øren et al., 1992). Oil layers were indeed observed in three-phase imaging experiments performed at immiscible conditions (Scanziani et al., 2018b) and no direct contact of gas and water was seen. However, the presence or absence of layers also depends on the curvatures of the fluid-fluid interfaces (van Dijke and Sorbie, 2003; van Dijke et al., 2004; van Dijke and Sorbie, 2007). A necessary condition for the presence of oil layers in a corner of the pore space, as illustrated in Fig. 5, is (Fenwick and Blunt, 1995):

$$\kappa_{mgo} < \kappa_{mow} \quad (1)$$

where κ_m is the mean curvature of the interface, which in Fig. 5 is assumed approximately to be the inverse of the radius of curvature, while the other radius – out of the plane of the figure – is much larger. Using the Young-Laplace equation:

$$P_c = 2\sigma\kappa_m \quad (2)$$

where σ is the interfacial tension between the two phases, Eq. (1) can be written as an inequality involving P_{cow} and P_{cgo} , the capillary pressures between oil-water and gas-oil phases respectively:

$$P_{cgo} < \frac{\sigma_{go}}{\sigma_{ow}} P_{cow} \quad (3)$$

The graphical representation of Eq. (3) is plotted in Fig. 5 using representative interfacial tension values. If the combination of P_{cow} and P_{cgo} falls above the critical line, oil layers cannot form. At near-miscible conditions, the ratio of σ_{go} to σ_{ow} is much lower compared to immiscible conditions. Therefore, the slope of the critical line is less steep and hence a much smaller P_{cgo} is sufficient to push oil layers out of the pore space.

2.2.5.2. Capillary Pressure measurement. To perform the analysis detailed in the previous section, we used the curvature-based capillary pressure measurement approach (Armstrong et al., 2012). The interfacial curvature between the fluids was measured from the segmented pore-scale images and then linked to the capillary pressure using the Young-Laplace equation, (2). We measured the curvatures of oil-water and gas-oil interfaces using a method previously presented in the literature (Armstrong et al., 2012; Andrew et al., 2014a; Li et al., 2018; Lin et al., 2018; Lin et al., 2019; Akai et al., 2019). First, a marching cube algorithm was used to extract oil-water and gas-oil interfaces from segmented images. The less wetting phase, oil in the case of an oil-water interface and gas in the case of a gas-oil interface, was smoothed using the unconstrained smoothing method (kernel size = 5) to remove the staircase-like nature of the voxelized images. The smoothed interfaces

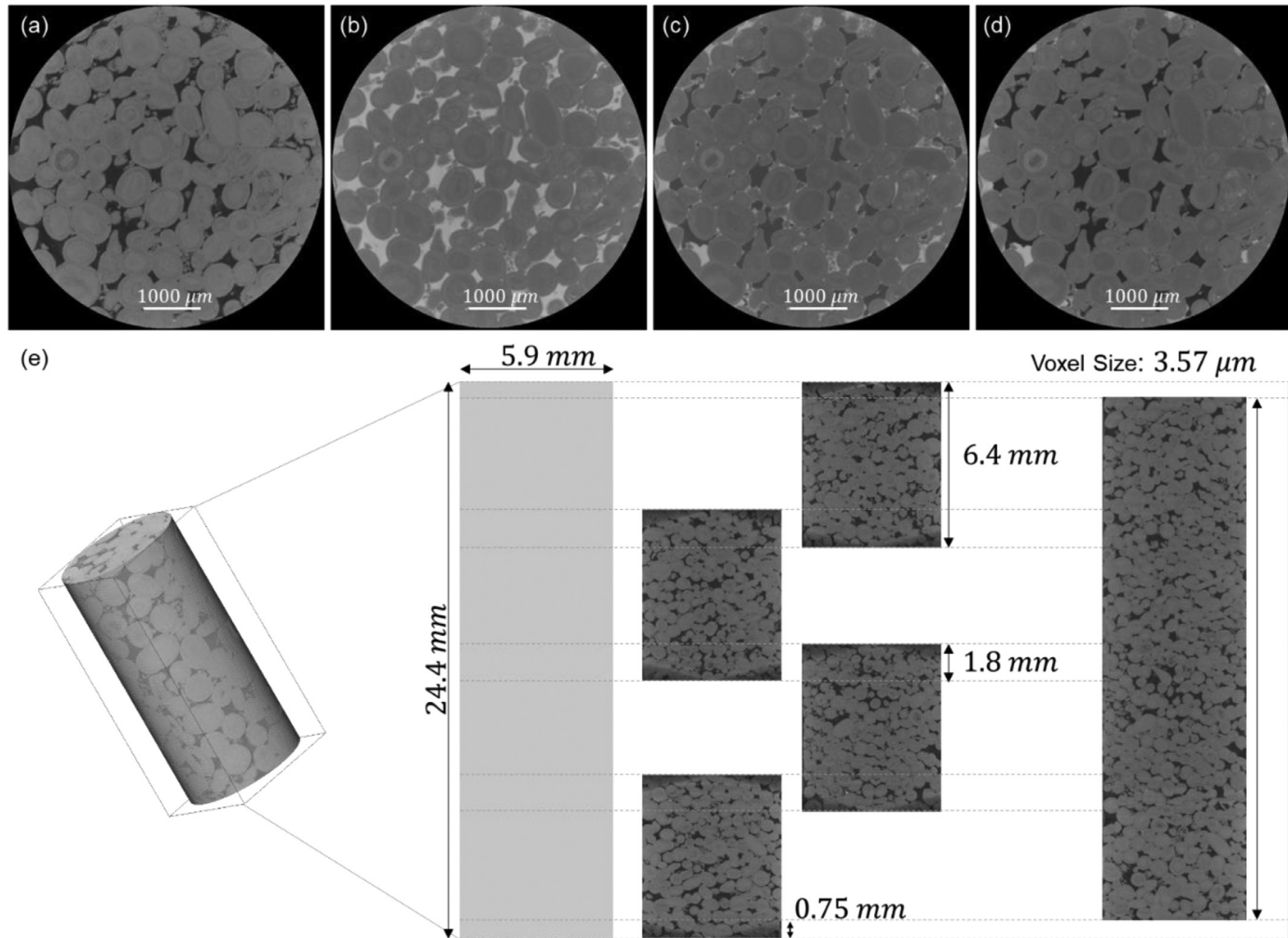


Fig. 4. A series of 2D slices with a voxel size of $3.57\text{ }\mu\text{m}$ for the Ketton sample showing the registered images to the dry scan in (a), after (b) water injection, (c) oil injection and (d) gas injection. (e) A schematic showing the location of the four scans taken to image the whole sample with the final stitched image.

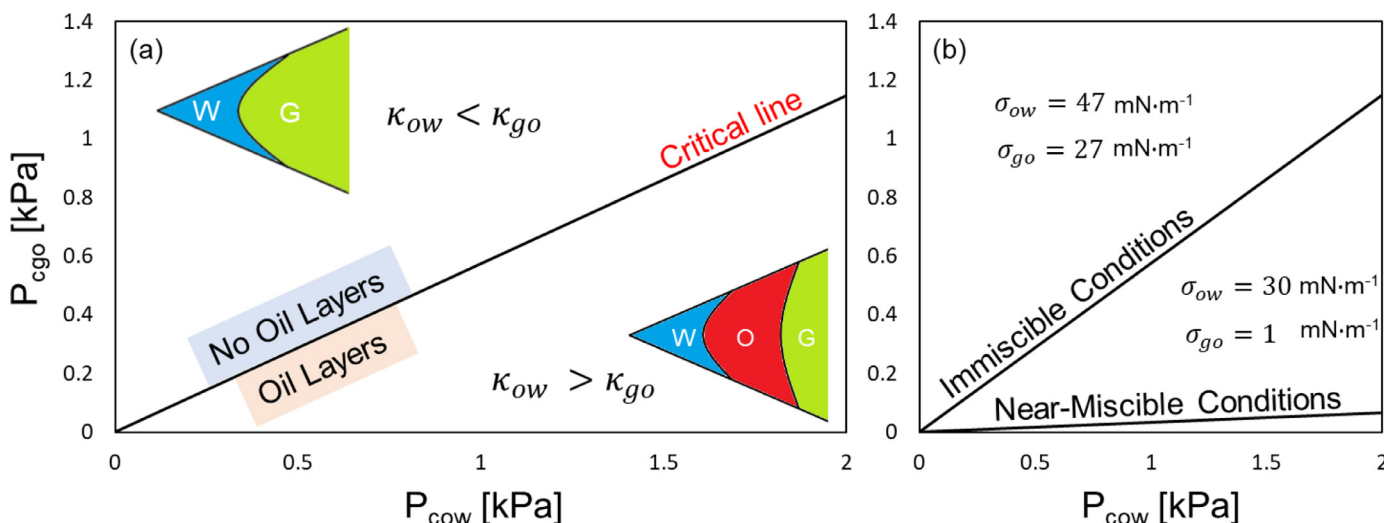


Fig. 5. A graphical representation of Eq. (3) that helps determine the likely presence or absence of oil layers in a spreading water-wet system depending on the microscopic oil-water and gas-oil capillary pressures. (a) The graph illustrates that if the ratio of P_{cgo} to P_{cow} falls above the critical line, oil layers will not form as P_{cgo} will squeeze out the oil-water interface ($\kappa_{ow} < \kappa_{go}$) and vice versa. (b) The critical line for the immiscible conditions studied by Scanziani et al. (2018b) is much steeper compared to near-miscible conditions and therefore it is more likely for oil layers to form for the same gas-oil capillary pressure.

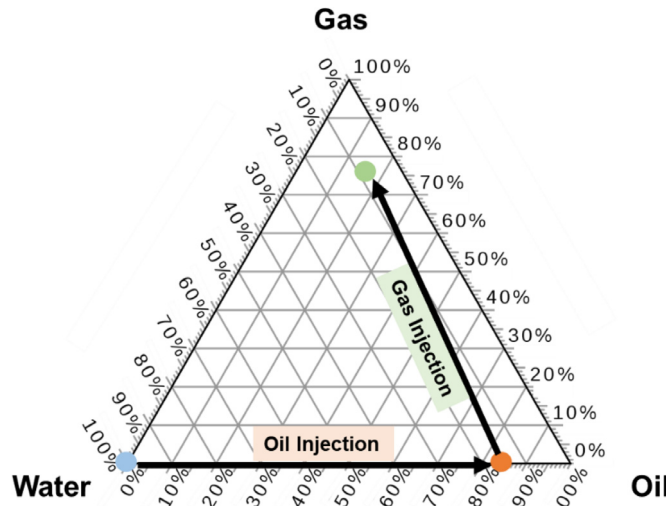


Fig. 6. A ternary diagram showing the end-point saturations of the three fluid phases after each injection step. Initially, the rock is fully saturated with water (blue point), then oil is injected in a primary drainage process until irreducible water saturation is reached (red point). Gas is then injected in a secondary recovery process resulting in the end-point saturations shown by the green point.

are then modelled as a quadratic form:

$$ax^2 + by^2 + cz^2 + 2exy + 2gyz + 2gxz + 2lx + 2my + 2nz + d = 0 \quad (5)$$

The eigenvalues and eigenvectors of this quadratic form correspond to the principal curvatures of the interfaces and their directions, respectively. The mean of these curvatures was then substituted alongside representative interfacial tension values into the Young-Laplace equation to calculate the microscopic oil-water and gas-oil capillary pressures.

3. Results and discussion

In Section 3.1, we start by quantifying the fluids saturations after each injection step. Then, we list the estimated oil-water, gas-water and oil-gas contact angles after near-miscible and immiscible gas injection in Section 3.2. In Section 3.3, the presence of oil layers and oil connectivity at near-miscible and immiscible conditions is investigated using the capillary pressure analysis described in Section 2.2.5.1 followed by an examination of the local oil thickness maps. In Sections 3.4 and 3.5, for near-miscible and immiscible conditions, we (i) quantify the interfacial area between the fluid phases and the fluid phases with the rock, and (ii) characterize the pore occupancy and visualize double displacement processes. For the comparisons in Sections 3.2–3.5, the experimental dataset of Scanziani et al. (2018b) for water-wet Ketton limestone is used to represent immiscible conditions.

3.1. Saturation Measurements

The saturation of each fluid phase in macro-porosity only was measured on the segmented images after each injection step. We assume that the micro-porosity remained water-saturated throughout the experiment. In the results presented below we have, for simplicity, ignored the contribution of micro-porosity to the saturation. The measured saturation end points are shown on the ternary diagram in Fig. 6. Initially, the sample was fully saturated with water (water saturation = 100%). Oil was then injected into the sample in a primary drainage process to form the initial reservoir conditions, with an oil saturation of 84% and 16% initial water saturation. Next, gas was injected in a secondary oil recovery process allowing for the production of both oil and water. At the end of the gas injection step, water, oil and gas saturations were 8%, 16% and 76% respectively. The injection of gas at near-

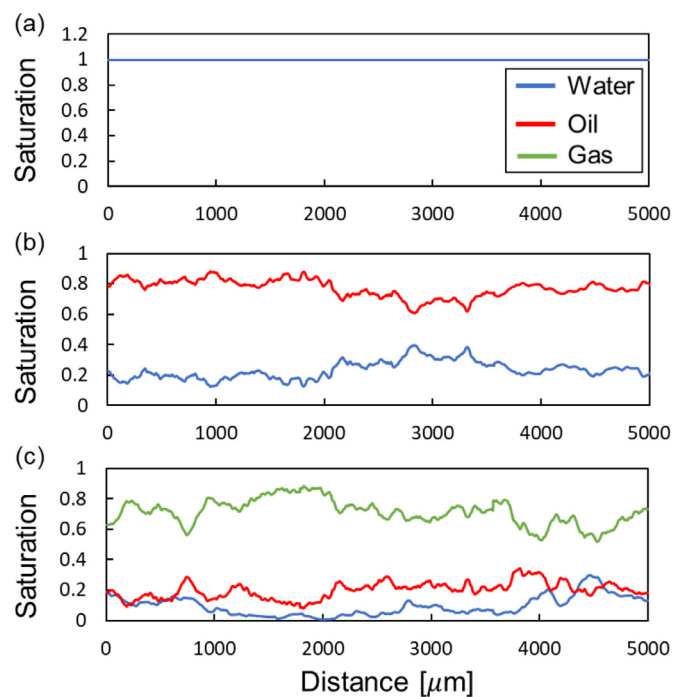


Fig. 7. The saturation profiles along the analysed region of the sample after (a) water injection, (b) oil injection, and (c) gas injection.

miscible conditions resulted in an oil recovery factor of 80%; this is significantly higher than that seen in a previous immiscible gas injection study by Scanziani et al. (2018b), where only 41% of oil was recovered after gas injection. However, it must be noted that in the case of Scanziani et al. (2018b), gas was injected in a tertiary recovery process rather than a secondary one. According to Iglaer et al. (2013), for a water-wet system, gas injection into a virgin oil reservoir leads to a lower residual oil saturation compared to the case where gas is injected after waterflooding. Nevertheless, the results show that the injection of gas in a secondary recovery process at near-miscible conditions can significantly improve oil recovery from the reservoir.

Given the large size of the stitched data, we selected the scan at the bottom of the sample for the subsequent analysis carried out in Sections 3.2–3.5. The saturation profile of each fluid along the analysed region of the sample was measured after each injection step, see Fig. 7. The profiles of all three-phases were consistent and showed no sign of capillary end effects throughout the whole injection sequence.

3.2. Contact Angles

The effective contact angles between oil and water (θ_{ow}), gas and oil (θ_{go}), and gas and water (θ_{gw}) were measured using the automated method developed by Scanziani et al. (2017) at near-miscible and immiscible conditions. In this method, the contact angle is measured between two fluids *in situ* on a plane perpendicular to the local three-phase contact line constructed from the segmented images. The measured contact angles are listed in Table 4. The high standard deviations are ascribed to contact angle hysteresis and pore-scale surface heterogeneities (e.g. surface roughness and pore geometry) (Andrew et al., 2014b).

The average oil-water contact angles at immiscible and near-miscible conditions, 48° and 52° respectively, indicate that the Ketton rock surfaces remained water-wet after oil and gas were injected into both systems. These measurements are in agreement with oil-water contact angles previously measured on similar rock-fluid systems (Singh et al., 2016). Furthermore, no evidence of wettability alteration was found upon exposure to X-ray radiation as seen by Brown et al. (2014).

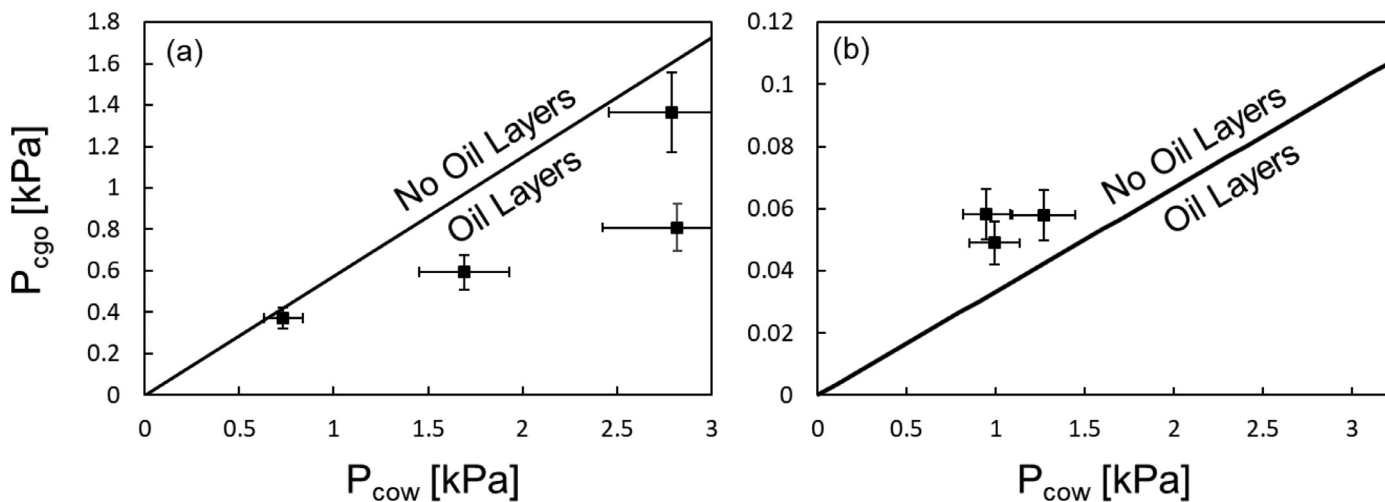


Fig. 8. Oil layer analysis conducted at (a) immiscible conditions and (b) near-miscible conditions. The graphs illustrate that under immiscible conditions oil layers are formed, while oil does not form layers under near-miscible conditions. Pressure data points in (a) from Scanziani et al. (2018b). Error bars indicate uncertainty in the measurements.

Table 4

Measured oil-water (θ_{ow}), gas-oil (θ_{go}), and gas-water (θ_{gw}) contact angles after gas injection at immiscible and near-miscible conditions together with the standard deviation of the measured values. The contact angles were measured *in situ* through the denser phase: water in the case of oil-water and gas-water contact angles, and oil in the case of the gas-oil contact angle. The contact angles were measured using the automated method developed by Scanziani et al. (2017). Immiscible contact angles from Scanziani et al. (2018b).

Miscibility State	Oil-Water	Gas-Oil	Gas-Water
Immiscible	$\theta_{ow} = 48 \pm 19^\circ$	$\theta_{go} = 0^\circ$	N/A
Near-miscible	$\theta_{ow} = 52 \pm 22^\circ$	$\theta_{go} = 73 \pm 17^\circ$	$\theta_{gw} = 52 \pm 18^\circ$

In immiscible conditions, the effective gas-oil contact angle is assumed to be zero since oil forms layers surrounding the gas phase. Furthermore, the formation of oil layers sandwiched between gas in the centre of the pore space and water in the corners prevents the gas phase from directly contacting the water phase, which makes it impossible to determine a gas-water contact angle.

At low gas-oil interfacial tensions (i.e. near-miscible conditions), oil and gas become similar fluids as they approach miscibility. Since oil and gas become similar, the rock will no longer necessarily have a strong affinity to be coated preferentially by oil over gas. Therefore, the strict wettability order in the system breaks down and oil and gas are allowed to flow along the same paths. This is evident from the large gas-oil contact angle measured at near-miscible conditions (73°), Table 4, which implies that the rock is neutrally wetting to oil and gas. It is further supported by the measured oil-water and gas-water contact angles at near-miscible conditions (Table 4), where both oil and gas formed the same effective contact angle (52°) with water. The measured interfacial tensions and contact angles satisfy the Bartell-Osterhof contact angle constraint for multiple phases in thermodynamic equilibrium to within uncertainties in our measurements (Bartell and Osterhof, 1927; Blunt, 2001).

3.3. Oil Layers and connectivity

Using the capillary pressure analysis described in Section 2.2.5.1, the likely presence of oil layers was investigated for water-wet Ketton limestone at near-miscible and immiscible gas injection conditions. The gas-oil and oil-water capillary pressures were measured on segmented images using the curvature-based approach detailed in Section 2.2.5.2.

The results are shown in Fig. 8. At immiscible conditions, the ratio of P_{cgo} to P_{cow} lies below the critical line suggesting the formation of stable oil layers sandwiched between the gas and water phases, see Fig. 8a, and indeed oil layers were seen surrounding the gas phase and preventing direct contact of gas and water (Scanziani et al., 2018b).

In contrast, during near-miscible gas injection, the P_{cgo} to P_{cow} ratio falls above the critical line suggesting that oil layers do not form (Fig. 8b); and indeed, we did not observe oil layers in the experiment – the gas, on injection, had sufficient pressure to push the oil from the pore space and oil layers were not seen. This confirms the micromodel observations of Williams and Dawe (1988) and Sohrabi et al. (2008) that oil does not spread in layers at near-miscible conditions even if the spreading coefficient is close to zero.

Fig. 9 shows grey-scale images of the pore space illustrating the presence and absence of oil layers at immiscible and near-miscible gas injection conditions respectively.

To examine the connectivity of the oil phase in the pore space, we obtained quantitative maps of the local oil phase thickness in 3D using the approach developed by Hildebrand and Rüegsegger (1997). The 3D oil thickness maps computed after gas injection at near-miscible and immiscible conditions are shown in Fig. 10. At near-miscible conditions, the residual oil phase existed as disconnected blobs residing in the corners of the pore space. However, for immiscible conditions, the oil phase was connected across the pore space by spreading layers with thicknesses that are of the order of 10 μm or larger. Furthermore, we computed thickness maps of the wetting water layers (Figure S2 in the supplementary material). No evidence was found of connected water wetting layers in the macro-pore space in our near-miscible water-wet system, as opposed to the immiscible system. The absence of water layers will further be discussed in Section 3.5.

The results show that no oil layers are formed under near-miscible conditions in a spreading water-wet system. This suggests that the oil displacement mechanism in the reservoir at near-miscible conditions is different than that of an immiscible one, where oil is produced by slowly draining the oil layers sandwiched between water and gas phases.

3.4. Interfacial Area

Since oil does not form layers at near-miscible conditions, gas can directly contact water in the pore space. To validate this assumption, we quantified the specific interfacial areas - area per unit volume – between: (i) the three fluid phases and (ii) each phase with the solid at near-miscible conditions and compared it to that at immiscible conditions,

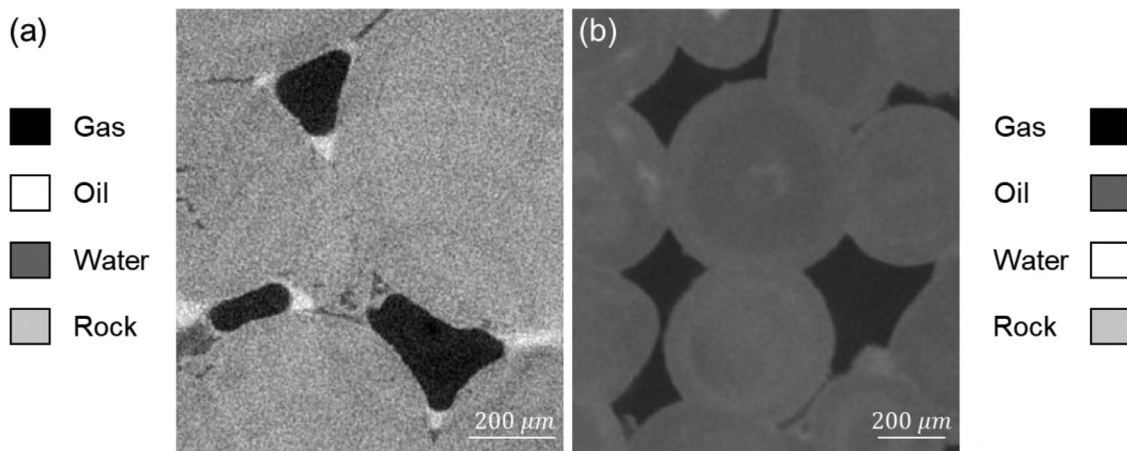


Fig. 9. (a) 2 μm resolution image of a water-wet Ketton sample showing the presence of oil layers at immiscible conditions after gas injection (Scanziani et al., 2018b). (b) 3.57 μm resolution image of a water-wet Ketton sample showing the absence of oil layers at near-miscible conditions after gas injection.

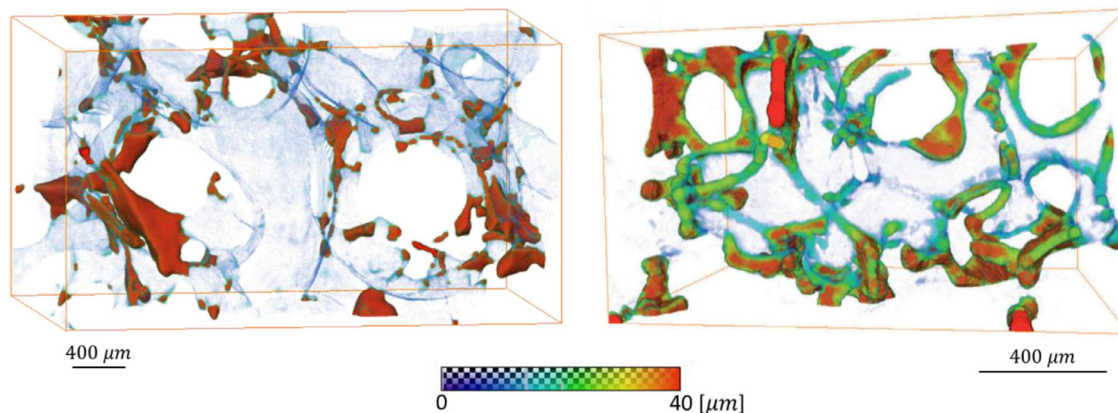


Fig. 10. The local thickness of the oil phase was computed at immiscible (right) and near-miscible (left) conditions. The oil phase was isolated and maximal balls were fitted to its structure to obtain the thickness maps at both conditions. Oil layer thickness map at immiscible conditions (right) from Scanziani et al. (2018b).

where there is no direct contact between gas and water. The measured interfacial areas are shown in Fig. 11. As expected, there is a rise in the area between gas and water at near-miscible conditions (Fig. 11a). However, there is a clear drop in the area between oil and water: this is caused by the absence of wetting layers which increase the oil-water interfacial area. The oil-gas specific area remains the highest at both injection conditions.

Despite the low gas-oil interfacial tension which makes a gas-oil interface more energetically favourable than the other pairs of fluids, the gas-oil interfacial area is much lower compared to the immiscible case: this is because spreading oil layers are absent. The oil-water interfacial area is also low, as there is less water retained in corners of the macro-pore space: there is more direct contact of oil with the solid which is evident in the larger oil-rock area and the smaller water-rock areas compared to the immiscible case. However, we do see some gas-water contacts which are absent at immiscible conditions.

3.5. Pore Occupancy and double displacement

To characterize the pore occupancy, we adopted the procedure developed by Scanziani et al. (2018b) which relies on the maximal ball (MB) method (Bultreys et al., 2015). First, the largest spheres that can occupy the pore space are found from the dry scan of the sample (Dong and Blunt, 2009; Raeini et al., 2017). The spheres are then imposed on the grey-scale images to find a relationship between the

dimensions of the pore and the phase occupying it. The pore occupancies obtained during the near-miscible and immiscible experiments are shown in Fig. 12.

As anticipated, during oil injection in water-wet systems, oil invades the largest pores, confining water to the smaller ones (Fig. 12a and b). The pore occupancy after gas injection at immiscible and near-miscible conditions are shown in Fig. 12c and d respectively. At immiscible conditions, gas, being the most non-wetting phase, invaded the centre of the larger pores, pushing oil into medium-sized pores, while water was squeezed into smaller pores (Blunt, 2017; Scanziani et al., 2018b), as expected based on the order of wettability.

The pore occupancy in near-miscible gas injection conditions is more intriguing, however: oil was displaced from large/medium-sized pores, replaced by gas and produced. Two noticeable movements happen during near-miscible gas injection: (i) oil is squeezed into a large fraction of the small-sized pores, and (ii) water is displaced from the smaller pores to occupy medium and large-sized pores. This results in a unique pore occupancy order at near-miscible conditions, where gas tends to reside in the largest pores, while oil and water occupy pores of varying sizes (small, medium and large).

The ability of oil and water to occupy pores of different sizes stems from several factors including: (i) oil does not form layers in the presence of gas and water; (ii) water is no longer confined in wetting layers; and (iii) double displacement processes.

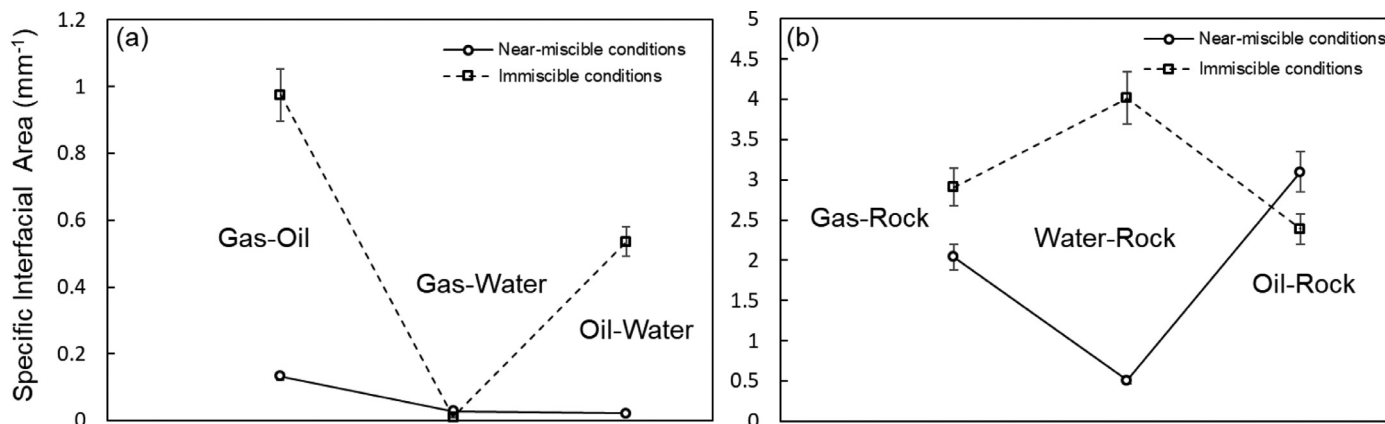


Fig. 11. Specific area measurements between (a) the three phases in the pore space and (b) each phase with the solid, at immiscible and near-miscible gas injection conditions. The specific area is calculated on extracted fluid-fluid and fluid-solid interfaces from segmented images. Error bars reflect uncertainties in the specific area measurement from one location to another. Gas, oil and water saturations at near-miscible conditions are $S_g = 0.76$, $S_o = 0.16$ and $S_w = 0.08$ respectively, while saturations at immiscible conditions are $S_g = 0.64$, $S_o = 0.22$ and $S_w = 0.14$. The different fluid saturations at both injection conditions might impact the measured interfacial areas.

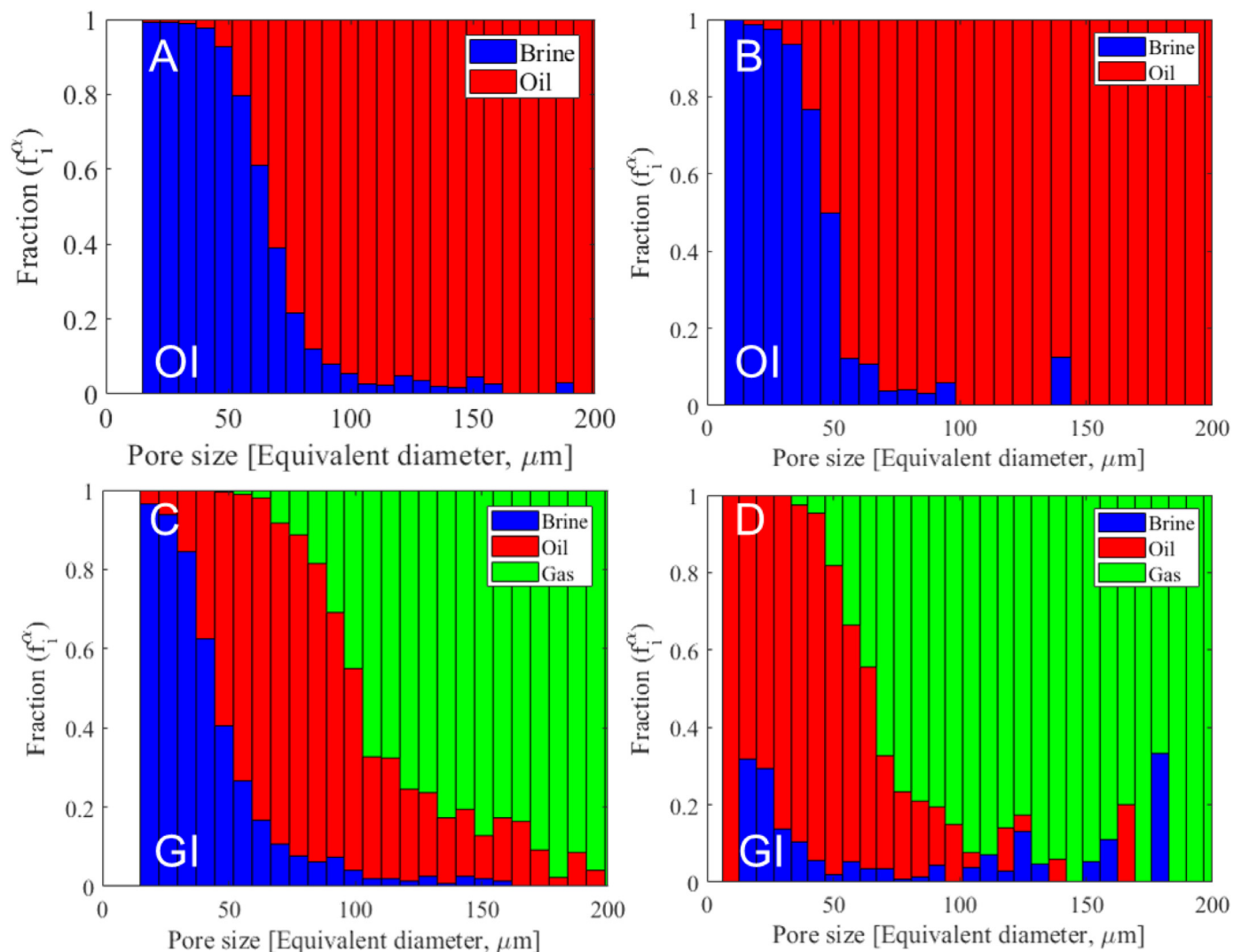


Fig. 12. Coloured bar charts representing the pore occupancy in the rock after oil injection at (A) immiscible conditions and (B) near-miscible conditions, and after gas injection at (C) immiscible conditions and (D) near-miscible conditions.

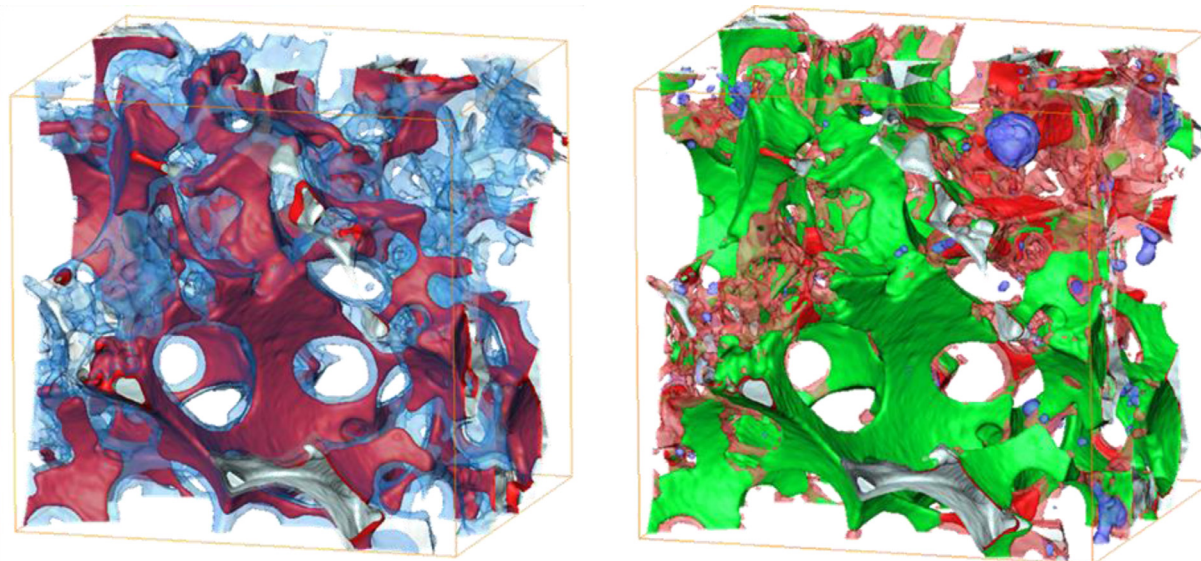


Fig. 13. A 3D representation of a selected subvolume ($1500 \times 1500 \times 1200 \mu\text{m}^3$) of the pore space showing how oil residing in the centres of the pore space after oil injection (left) is pushed into the corners of the pore space after gas injection (right), occupying a large fraction of the smaller pores. This prevents the formation of connected water wetting layers in the corners of the pore space. Water is shown in blue, oil prior to gas injection in dark red, oil post gas injection in light red, and gas in green. The rock has been rendered transparent in both images.

In both experiments, the principal overall displacement is oil by gas. In the immiscible experiment, where oil surrounds the gas phase, this occurs exclusively by direct removal of oil by gas: gas replaces oil in the larger pores as evident in Fig. 12c. In contrast, in the near-miscible experiment, we can have gas displacing oil in a double displacement process (Øren et al., 1992; Keller et al., 1997), where gas displaces water that displaces oil. The overall result is to increase the saturation of gas and displace oil, but here water changes its pore occupancy. It is evident from Fig. 12d, that gas displaces water in some of the smaller pore spaces – where it resides after oil injection – and then this water displaces oil in larger pores. The result is that water now appears, after gas injection, to reside in larger pores than it occupied after oil injection.

There is also a modest amount of displacement of water by gas in the immiscible experiment, here, gas directly displaces water from the larger water-filled elements. Furthermore, it is possible to have a double drainage process, where gas displaces oil that displaces water. In this case, it is the pore occupancy of oil that changes. For the immiscible experiment, see Fig. 12c, the tendency is for oil to be pushed out of the larger pores by gas and then displace water from smaller elements. However, for the near-miscible experiment, we see the same process, but where oil is pushed into some of the very smallest pores which tends to disconnect the water, as evident in Fig. 13.

The results show that the fluid pore occupancy in a water-wet system is altered when switching from immiscible to near-miscible conditions. This is likely to have a direct impact on the three-phase relative permeability of the system compared to the immiscible case with potentially lower oil and water relative permeability at low saturation, but a high oil relative permeability at intermediate saturation to facilitate the favourable recovery seen.

Furthermore, the most significant impact of oil layers is that they provide a mechanism for the displacement of waterflood residual oil, which enables the recovery of oil down to very low saturations. Therefore, if oil does not spread at near-miscible conditions, how is it recovered if gas is injected in a tertiary recovery process? Perhaps near-miscible gas injection is only more efficient if implemented as a secondary recovery process. Moreover, the presence of spreading oil layers enables efficient trapping of gas during subsequent water injections – in near-miscible systems there may be less gas trapping.

4. Conclusions and future work

We have provided a detailed 3D *in situ* pore-scale analysis of near-miscible three-phase flow at elevated temperature and pressure in a water-wet carbonate rock. In particular, we investigated the (i) presence of oil and water layers, (ii) fluid-fluid and fluid-solid interfacial areas, (iii) pore occupancy, and (iv) double displacement processes at near-miscible conditions and compared these results to observations made at immiscible conditions by Scanziani et al. (2018b). The three phases were injected in the rock in the following order: (i) water injection, (ii) primary oil drainage, and (iii) secondary gas injection. We observed distinct pore-scale phenomena at near-miscible conditions, suggesting that it is a unique displacement process and cannot be represented by models developed for immiscible displacement.

The main findings of the study can be summarized as follows:

1. A substantial amount of oil can be recovered by secondary gas injection at near miscible conditions (up to 80% recovery factor). This is attributed to two reasons: (i) gas displaces oil efficiently from the pores (100% microscopic displacement efficiency) due to the low gas-oil interfacial tension, and (ii) the displaced oil flows rapidly in the centre of the larger pores, as it is no longer confined to movement in layers, until it gets produced.
2. The rock becomes neutrally wetting to gas and oil as they become similar fluids at near-miscible conditions; the strict wettability order in the system breaks down. This facilitates the flow of gas and oil along the same path in the pore space. Oil and gas have similar contact angles with water.
3. Oil does not form layers between oil and gas in a water-wet system at near-miscible conditions, despite having a spreading coefficient close to zero. The gas-oil capillary pressure is sufficiently high to squeeze oil out of layers, while oil itself is not strongly wetting to gas (point 2).
4. A series of gas-oil-water and gas-water-oil double displacement events were observed. Gas-water-oil displacement enables water to be pushed into larger pores.
5. The pore occupancy order is altered at near-miscible conditions, while gas tends to reside in the largest pores, oil and water occupy pores of varying sizes (small, medium and large).

6. Oil displaces water from the small-sized pores preventing the formation of a connected wetting layer throughout the macro-pore space.
7. The altered interfacial tensions at near-miscible conditions impact the fluid arrangement in the pore space, resulting in a high oil-gas relative interfacial area and lower, but similar, oil-water and gas-water interfacial areas in the pore space.

Future work on near-miscible gas injection could focus on: (i) investigating the pore occupancy of mixed-wet and oil-wet systems; (ii) determining the range of minimum miscibility pressures under which these conditions persist with a series of experiments conducted for a range of gas-oil interfacial tensions; (iii) implementing near-miscible injection in a tertiary recovery process as discussed above; and (iv) characterizing three-phase relative permeabilities at such conditions. Furthermore, a time-resolved synchrotron experiment could be conducted to characterize the pore-scale dynamics of a near-miscible displacement process. These experiments could serve as the foundation stones to pore-scale modelling and field simulations of near-miscible gas injection processes.

Declaration of Competing Interest

None

CRediT authorship contribution statement

Abdulla Alhosani: Conceptualization, Investigation, Formal analysis, Writing - original draft, Writing - review & editing. **Alessio Scanziani:** Conceptualization, Investigation, Formal analysis. **Qingyang Lin:** Conceptualization, Investigation, Formal analysis. **Ziqing Pan:** Investigation, Formal analysis. **Branko Bijeljic:** Conceptualization, Supervision, Formal analysis. **Martin J. Blunt:** Conceptualization, Supervision, Formal analysis.

Acknowledgements

We acknowledge Abu Dhabi National Oil Company (ADNOC) for funding this study.

Supplementary material

Supplementary material associated with this article can be found, in the online version, at doi:[10.1016/j.advwatres.2019.103432](https://doi.org/10.1016/j.advwatres.2019.103432).

References

- Akai, T., Lin, Q., Alhosani, A., Bijeljic, B., Blunt, J.M., 2019. Quantification of uncertainty and best practice in computing interfacial curvature from complex pore space images. *Materials* 12, 2138.
- Andrew, M., Bijeljic, B., Blunt, M.J., 2014a. Pore-By-Pore capillary pressure measurements using X-Ray microtomography at reservoir conditions: curvature, snap-off, and remobilization of residual CO₂. *Water Resour. Res.* 50, 8760–8774.
- Andrew, M., Bijeljic, B., Blunt, M.J., 2014b. Pore-Scale contact angle measurements at reservoir conditions using X-Ray microtomography. *Adv. Water Resour.* 68, 24–31.
- Armstrong, R.T., Porter, M.L., Wildenschild, D., 2012. Linking pore-scale interfacial curvature to column-scale capillary pressure. *Adv. Water Resour.* 46, 55–62.
- Bartell, F.E., Osterhof, H.J., 1927. Determination of the wettability of a solid by a liquid: relation of adhesion tension to stability of color varnish and lacquer systems. *Ind. Eng. Chem.* 19, 1277–1280.
- Bijeljic, B., Mostaghimi, P., Blunt, M.J., 2013. Insights into non-Fickian solute transport in carbonates. *Water Resour. Res.* 49, 2714–2728.
- Bijeljic, B., Raeini, A.Q., Lin, Q. & Blunt, M.J. 2018. Multimodal functions as flow signatures in complex porous media. arXiv:1807.07611.
- Blunt, M.J., 2001. Constraints on contact angles for multiple phases in thermodynamic equilibrium. *J. Colloid Interface Sci.* 239, 281–282.
- Blunt, M.J., 2017. Multiphase Flow in Permeable Media: A Pore-Scale Perspective. Cambridge University Press.
- Brown, K., Schlüter, S., Sheppard, A., Wildenschild, D., 2014. On the challenges of measuring interfacial characteristics of three-phase fluid flow with X-Ray microtomography. *J. Microsc.* 253, 171–182.
- Bui, L.H., Tsau, J.-S., Willhite, G.P., 2010. Laboratory investigations of CO₂ near miscible application in arbuckle reservoir. *Proceeding of The SPE Improved Oil Recovery Symposium Society of Petroleum Engineers*, No. 129710.
- Bultreys, T., Van Hoorebeke, L., Cnudde, V., 2015. Multi-Scale, micro-computed tomography-based pore network models to simulate drainage in heterogeneous rocks. *Adv. Water Resour.* 78, 36–49.
- Burger, J.E., Rao, B., Mohanty, K.K., 1994. Effect of phase behavior on bypassing in enriched gasflows. *SPE Reserv. Eng.* 9 (25254), 112–118.
- Chen, H., Zhang, X., Chen, Y., Tang, H., Mei, Y., Li, B., Shen, X., 2017. Study on pressure interval of near-miscible flooding by production gas Re-injection in QHD offshore oilfield. *J. Pet. Sci. Eng.* 157, 340–348.
- Dong, H., Blunt, M.J., 2009. Pore-Network extraction from micro-computerized-tomography images. *Phys. Rev. E* 80, 036307.
- Fenwick, D.H., Blunt, J.M., 1995. Pore level modelling of three phase flow in porous media. In: *Ior 1995 - Proceedings Of The 8th European Symposium On Improved Oil Recovery*. Vienna, Austria.
- Georgiadis, A., Llovel, F., Bismarck, A., Blas, F.J., Galindo, A., Maitland, G.C., Trusler, J.P.M., Jackson, G., 2010. Interfacial tension measurements and modelling of (Carbon Dioxide+n-alkane) and (Carbon Dioxide+water) binary mixtures at elevated pressures and temperatures. *J. Supercrit. Fluid.* 55, 743–754.
- Grigg, R.B., Schechter, D.S., 1997. State of the industry in CO₂ floods. In: *Proceedings of The SPE Annual Technical Conference and Exhibition*. San Antonio, Texas Society Of Petroleum Engineers, No. 38849.
- Heidaryan, E., Hatami, T., Rahimi, M., Moghadasi, J., 2011. Viscosity of pure Carbon Dioxide at supercritical region: measurement and correlation approach. *J. Supercrit. Fluid.* 56, 144–151.
- Hildebrand, T., Rüegsegger, P., 1997. A new method for the model-independent assessment of thickness in three-dimensional images. *J. Microsc.* 185, 67–75.
- Iglauer, S., Paluszny, A., Blunt, M.J., 2013. Simultaneous oil recovery and residual gas storage: a pore-level analysis using *in situ* X-Ray micro-tomography. *Fuel* 103, 905–914.
- Jamilolahmady, M., Danesh, A., Tehrani, D.H., Duncan, D.B., 2000. A mechanistic model of gas-condensate flow in pores. *Transp. Porous Media* 41, 17–46.
- Jones, T.R., Carpenter, A., Golland, P., 2005. Voronoi-Based segmentation of cells on image manifolds. In: Liu, Y., Jiang, T., Zhang, C. (Eds.), *Computer Vision for Biomedical Image Applications*, 2005. Springer Berlin Heidelberg, Berlin, Heidelberg, pp. 535–543.
- Keller, A.A., Blunt, M.J., Roberts, A.P.V., 1997. Micromodel observation of the role of oil layers in three-phase flow. *Transp. Porous Media* 26, 277–297.
- Li, T., Schlüter, S., Dragila, M.I., Wildenschild, D., 2018. An improved method for estimating capillary pressure from 3D microtomography images and its application to the study of disconnected nonwetting phase. *Adv. Water Resour.* 114, 249–260.
- Li, X., Boek, E., Maitland, G.C., Trusler, J.P.M., 2012. Interfacial tension of (Brines + CO₂): (0.864 NaCl + 0.136 KCl) at temperatures between (298 and 448) K, pressures between (2 and 50) MPa, and total molalities of (1 to 5) mol·kg⁻¹. *J. Chem. Eng. Data* 57, 1078–1088.
- Lin, Q., Al-Khulaifi, Y., Blunt, M.J., Bijeljic, B., 2016. Quantification of sub-resolution porosity in carbonate rocks by applying high-salinity contrast brine using X-Ray microtomography differential imaging. *Adv. Water Resour.* 96, 306–322.
- Lin, Q., Bijeljic, B., Berg, S., Pini, R., Blunt, M.J., Krevor, S., 2019. Minimal surfaces in porous media: pore-Scale imaging of multiphase flow in an altered-wettability ben-themer sandstone. *Phys. Rev. E* 99, 063105.
- Lin, Q., Bijeljic, B., Pini, R., Blunt, M.J., Krevor, S., 2018. Imaging and measurement of pore-scale interfacial curvature to determine capillary pressure simultaneously with relative permeability. *Water Resour. Res.* 54, 7046–7060.
- Longeron, D.G., 1980. Influence of very low interfacial tensions on relative permeability. *Soc. Pet. Eng. J.* 20 (129710), 391–401.
- Moghadasi, L., Guadagnini, A., Inzoli, F., Bartosek, M., Renna, D., 2016. Characterization of two- and three-phase relative permeability of water-wet porous media through X-Ray saturation measurements. *J. Pet. Sci. Eng.* 145, 453–463.
- Nist. 2019. Reference fluid thermodynamic and transport properties database (Ref-prop)[Online]. Available: <https://www.Nist.Gov/Srd/Refprop> [Accessed July 3, 2019].
- Ören, P.E., Billiotte, J., Pinczewski, W.V., 1992. Mobilization of waterflood residual oil by gas injection for water-wet conditions. *SPE Form. Eval.* 7 (20185), 70–78.
- Pande, K.K., 1992. Effects of gravity and viscous crossflow on hydrocarbon miscible flood performance in heterogeneous reservoirs. In: *Proceedings of The SPE Annual Technical Conference and Exhibition*. Washington, D.C. No. 24935.
- Raeini, A.Q., Bijeljic, B., Blunt, M.J., 2017. Generalized network modeling: network extraction as a coarse-scale discretization of the void space of porous media. *Phys. Rev. E* 96, 013312.
- Scanziani, A., Alhammadi, A., Bijeljic, B., Blunt, M.J., 2018a. Three-Phase flow visualization and characterization for a mixed-wet carbonate rock. In: *Abu Dhabi International Petroleum Exhibition Conference*. Abu Dhabi, Uae Proceedings Of The SPE.
- Scanziani, A., Singh, K., Blunt, M.J., Guadagnini, A., 2017. Automatic method for estimation of *in situ* effective contact angle from X-Ray micro tomography images of two-phase flow in porous media. *J. Colloid Interface Sci.* 496, 51–59.
- Scanziani, A., Singh, K., Bultreys, T., Bijeljic, B., Blunt, M.J., 2018b. *In situ* characterization of immiscible three-phase flow at the pore scale for a water-wet carbonate rock. *Adv. Water Resour.* 121, 446–455.
- Schechter, D.S., Grigg, R., Guo, B., Schneider, B., 1998. Wellman unit CO₂ flood: reservoir pressure reduction and flooding the water/oil. In: *Proceedings of The SPE Annual Technical Conference And Exhibition*. New Orleans, Louisiana No. 48948.
- Sheppard, A.P., Sok, R.M., Averdunk, H., 2004. Techniques for image enhancement and segmentation of tomographic images of porous materials. *Phys. A: Stat. Mech. Its Appl.* 339, 145–151.

- Shyeh-Yung, J.G.J., 1991. Mechanisms of miscible oil recovery: effects of pressure on miscible and near-miscible displacements of oil by Carbon Dioxide. SPE Annual Technical Conference and Exhibition. Society of Petroleum Engineers No. 22651.
- Singh, K., Bijelic, B., Blunt, M.J., 2016. Imaging of oil layers, curvature and contact angle in a mixed-wet and a water-wet carbonate rock. *Water Resour. Res.* 52, 1716–1728.
- Sohrabi, M., Danesh, A., Tehrani, D.H., Jamiolahmady, M., 2008. Microscopic mechanisms of oil recovery by near-miscible gas injection. *Transp. Porous. Media* 72, 351–367.
- Thomas, F.B., Holowach, N., Zhou, X., Bennion, D.B., Bennion, D.W., 1994. Miscible or near-miscible gas injection, which is better? In: Proceedings of The SPE/DOE Improved Oil Recovery Symposium. Tulsa, Oklahoma No. 55563.
- Van Dijke, M.I.J., Lago, M., Sorbie, K.S., Araujo, M., 2004. Free energy balance for three fluid phases in a capillary of arbitrarily shaped cross-section: capillary entry pressures and layers of the intermediate-wetting phase. *J. Colloid Interface Sci.* 277, 184–201.
- Van Dijke, M.I.J., Sorbie, K.S., 2007. Consistency of three-phase capillary entry pressures and pore phase occupancies. *Adv. Water Resour.* 30, 182–198.
- Van Dijke, M.I.J., Sorbie, K.S., 2003. Three-Phase capillary entry conditions in pores of noncircular cross-section. *J. Colloid Interface Sci.* 260, 385–397.
- Vinegar, H.J., Wellington, S.L., 1987. Tomographic imaging of three-phase flow experiments. *Rev. Sci. Instrum.* 58, 96–107.
- Williams, J.K., Dawe, R.A., 1988. Photographic observations of unusual flow phenomena in porous media at interfacial tensions below 0.1 mN m^{-1} . *J. Colloid Interface Sci.* 124, 691–696.
- Wylie, P., Mohanty, K.K., 1997. Effect of water saturation on oil recovery by near-miscible gas injection. *SPE Reserv. Eng.* 12 (36718), 264–268.